International Journal of Solids and Structures 48 (2011) 611–624

Contents lists available at ScienceDirect

International Journal of Solids and Structures

journal homepage: www.elsevier.com/locate/ijsolstr

A combined analytical, numerical, and experimental study of shape-memory-alloy helical springs

Reza Mirzaeifar [a], Reginald DesRoches [b], Arash Yavari [b,*]

[a] George W. Woodruff School of Mechanical Engineering, Georgia Institute of Technology, Atlanta, GA 30332, USA
[b] School of Civil and Environmental Engineering, Georgia Institute of Technology, Atlanta, GA 30332, USA

ARTICLE INFO

Article history:
Received 21 May 2010
Received in revised form 8 September 2010
Available online 31 October 2010

Keywords:
Shape memory alloy (SMA)
Torsion
Helical spring
Pseudoelastic

ABSTRACT

In this paper, the pseudoelastic response of shape memory alloy (SMA) helical springs under axial force is studied both analytically and numerically. In the analytical solution two different approximations are considered. In the first approximation, both the curvature and pitch effects are assumed to be negligible. This is the case for helical springs with large ratios of mean coil radius to the cross sectional radius (spring index) and small pitch angles. Using this assumption, analysis of the helical spring is reduced to that of the pure torsion of a straight bar with circular cross section. A three-dimensional phenomenological macroscopic constitutive model for polycrystalline SMAs is reduced to the one-dimensional pure shear case and a closed-form solution for torsional response of SMA bars in loading and unloading is obtained. In the next step, the curvature effect is included and the SMA helical spring is analyzed using the exact solution presented for torsion of curved SMA bars. In this refined solution, the effect of the direct shear force is also considered. In the numerical analyses, the three-dimensional constitutive equations are implemented in a finite element method and using solid elements the loading–unloading of an SMA helical spring is simulated. Analytical and numerical results are compared and it is shown that the solution based on the SMA curved bar torsion gives an accurate stress analysis in the cross section of the helical SMA spring in addition to the global load–deflection response. All the results are compared with experimental data for a Nitinol helical spring. Several case studies are presented using the proposed analytical and numerical solutions and the effect of changing different parameters such as the material properties and temperature on the loading–unloading hysteretic response of SMA helical springs is studied. Finally, some practical recommendations are given for improving the performance of SMA helical springs used as energy dissipating devices, for example for seismic applications.

1. Introduction

Since the first observation of the shape memory effect (SME) in some alloys (Chang and Read, 1951a,b), studying shape memory alloys (SMAs) has been an active field of research. The unique ability of shape memory alloys in recovering large inelastic strains and also generating high stresses has caused a considerable increase in manufacturing devices made of these materials in recent years. The SMAs are now used in applications in a wide variety of devices ranging from simple parts like cell phone antennas or eyeglass frames to complicated devices in mechanical (Brook, 1983; Jee et al., 2006; Xua and Song, 2004), biomechanical (Petrini et al., 2005), aerospace (Hartl and Lagoudas, 2007), and civil engineering (DesRoches and Smith, 2004).

The unique macroscopic properties of SMAs are based on the solid–solid phase transition of the underlying lattice between a high symmetry cubic lattice (austenite) and a low symmetry lattice (martensite). It is known that when the SMA atoms are arranged in the cubic austenite lattice form, the entropy and internal energy are higher compare to the martensite lattice. The competition between the entropy and internal energy is reflected in the free energy $F = U - TS$, where U is the internal energy, S is the entropy and T is temperature. It is known that at higher temperatures the entropy overcomes the competition and the austenite phase is preferred while at lower temperatures the internal energy determines the stability and the martensite phase is preferred (Kastner, 2003, 2006). For a comprehensive discussion on general properties of SMAs and the phase transformation phenomenon, readers are referred to Müller and Xu (1991) and Müller and Seelecke (2001).

As a result of the solid–solid phase transformation (usually called martensitic phase transformation), and according to the specific way the transformation occurs, SMAs exhibit two significant macroscopic phenomena: the shape memory effect and pseudoelasticity. Each of these two macroscopic responses to mechanical and/or thermal loading is the origin of a vast range of applications

* Corresponding author.
E-mail address: arash.yavari@ce.gatech.edu (A. Yavari).

0020-7683/$ - see front matter © 2010 Elsevier Ltd. All rights reserved.
doi:10.1016/j.ijsolstr.2010.10.026

for SMAs. In this paper we focus on the pseudoelasticity of SMAs. This phenomenon occurs when the austenite phase is loaded isothermally to full transformation to detwinned martensite and then unloaded to the stress free state. During loading, after an initial elastic response, a large amount of inelastic deformation strain is produced. By unloading, strain is completely recovered during transformation of martensite back to the austenite. Note that the load–deflection response during a pseudoelastic loading–unloading is temperature dependent.

While searching for new shape memory alloys for improving their pseudoelastic response is still an active field of research (Tanaka et al., 2010; Voit et al., 2010), a large effort has been made by many researchers to introduce more precise analytical and numerical methods for analyzing pseudoelastic and SME response of SMA structures. Some of these studies focus on introducing constitutive equations to model SMA response to mechanical and thermal loads more accurately (see Liang and Rogers, 1992; Tanaka et al., 1995; Boyd and Lagoudas, 1996; Bo and Lagoudas, 1999; Qidwai and Lagoudas, 2000a; Popov and Lagoudas, 2007; Arghavani et al., 2010) while others focus on numerical (Mirzaeifar et al., 2009), semi-analytical (Mirzaeifar et al., in press), and exact solutions (Mirzaeifar et al., 2010).

The pseudoelastic response of SMAs is hysteretic. This phenomenon provides ideal energy dissipating and damping capabilities for SMAs and enables them to be used in passive control of structures under earthquake loads. DesRoches and Delemont (2002) investigated the effectiveness of shape memory alloy restrainer bars to reduce the seismic vulnerability of bridges. DesRoches and Smith (2004) provided a critical review of the state-of-the-art in the use of shape memory alloys for applications in seismic resistant design. McCormick et al. (2006) studied seismic vibration control using superelastic shape memory alloys by considering NiTi wires and bars. Auricchio et al. (2006) studied the damping properties of SMAs numerically and experimentally by considering uniaxial loading of SMA bars and wires of different size and chemical composition. Recently, Speicher et al. (2009) proposed a new device with an SMA helical spring as a potential bracing element in buildings. It is shown that this device can be used as an efficient recentering system to improve the performance of structures during seismic events.

During an earthquake event, the helical spring device will likely see 20–25 cycles into the transformation stress range, depending on the properties of the structure in which it is being used, and the magnitude of the ground shaking. It is well known that SMAs experience changes in behavior (typically referred to as the fatigue effect) with increased cycling resulting in an accumulation of irreversible strain and a slight decrease in forward transformation stress. Previous studies by the second author have shown that these changes have minimal effect on the resulting behavior of the system in which the SMA is used (Andrawes and DesRoches, 2008). Moreover, this effect can be minimized by mechanical training of the SMA material prior to implementation in the device (McCormick and DesRoches, 2006). In this paper, we will not consider the fatigue effect in analyzing the SMA springs. The necessity of having an accurate analytical and numerical modeling of the proposed SMA device besides its vast applications (Dong et al., 2008; Liang and Rogers, 1997; Lee et al., 2009) motivated the authors to seek analytical and numerical solutions for these springs.

In one of the first studies of SMA helical springs, Tobushi and Tanaka (1991) analyzed a helical spring under axial load assuming that each small segment is in pure torsion. They used Tanaka's constitutive model (Tanaka, 1986) but in the stress–strain relation the hardening during phase transformation is ignored and the material is treated as perfectly plastic. Although this assumption simplifies the solution remarkably, experimental results show that the hardening response in stress–strain relations for polycrystalline SMAs cannot be ignored. In another effort Toi et al. (2004) modified the Brinson's one-dimensional constitutive model (Brinson, 1993) and implemented it in an incremental finite element formulation using Timoshenko beam elements. In their study, SMA helical springs are modeled numerically and simulation outputs are compared with experimental results. Using beam elements for analysis of helical springs decreases the computational time remarkably but an accurate stress analysis cannot be done and as we will see in the sequel, the stress and martensitic volume fraction distributions in the cross section of SMA helical springs cannot be captured using beam elements.

In this paper, we propose three different analysis strategies besides the experimental results for SMA helical springs subjected to axial load. The simplest method for analyzing helical springs is to assume that each portion of the spring acts as a straight bar under torsion. It can be shown that when the spring index (the ratio of mean coil radius to the cross section radius) is large and the helix angle is small, this assumption leads to fairly accurate results (Wahl, 1944). Readers are referred to Ancker and Goodier (1958a,b,c) for a detailed discussion on the accuracy of this assumption and modifications to obtain a more accurate solution for elastic helical springs considering the curvature and pitch effects. In the present study, as the first approximation we introduce an exact solution for analysis of SMA helical springs by ignoring the curvature and pith effects. Although the analysis of helical springs based on the straight bar torsion model (SBTM) is of enough accuracy for most practical helical elastic springs, it will be shown that in the case of an SMA spring, curvature plays a significant rule and an accurate stress analysis in the cross section cannot be obtained based on SBTM. On the other hand, nearly all the practical helical springs have small to large spring indices but small pitch angles (Wahl, 1944). In order to capture a more accurate stress analysis and to cover a wider range of practical springs, the curvature correction is added to SBTM and a curved bar torsion model (CBTM) is presented. In addition to these two analytical models, a three-dimensional finite element simulation method is developed for analysis of SMA helical springs. Experimental test data on a Nitinol spring subjected to axial compression are compared with the analytical, and numerical results, the accuracy of each method in predicting the global force–displacement and stress analysis is investigated. It is shown that the SBTM calculates the global force–displacement response with good accuracy but for precise stress and martensitic volume fraction distributions, the curvature correction should be used. Both analytical methods are remarkably fast compared to the finite element simulations and can be used for studying the effect of changing any of the material or geometrical parameters on the spring response even for an optimization process that needs a large number of simulations. In the numerical results, in addition to the comparisons that are presented for studying the accuracy of different proposed methods, many case studies are presented for studying the effect of changing material parameters and the ambient temperature on the spring hysteretic response. Finally, some recommendations are made for improving SMA springs as dampers and energy absorbing devices.

This paper is organized as follows. In Section 2 a general three-dimensional constitutive equation for polycrystalline SMAs and a one-dimensional reduced constitutive equation for pure torsion are briefly reviewed. In Section 3 two analytical methods based on the exact solution for pure torsion of a straight SMA bar and the torsion of a curved SMA bar for analyzing SMA helical springs are presented. The experimental set-up and data for the SMA helical spring are discussed in Section 4 and the details of finite element simulations are given in Section 5. Several case studies are presented in Section 6 and a comparison is made between the proposed methods for stress and load–deflection analysis of SMA

helical springs. Material uncertainty is studied and practical recommendations for improving SMA helical springs as energy absorbing and damping devices are given. The effect of ambient temperature on the spring response is also studied. Conclusions are given in Section 7.

2. SMA constitutive equations

The total Gibbs free energy G for polycrystalline SMAs is given by Boyd and Lagoudas (1996) and Qidwai and Lagoudas (2000a):

$$G(\boldsymbol{\sigma},T,\boldsymbol{\epsilon}^t,\xi) = -\frac{1}{2\rho}\boldsymbol{\sigma}:\mathbb{S}:\boldsymbol{\sigma} - \frac{1}{\rho}\boldsymbol{\sigma}:[\boldsymbol{\alpha}(T-T_0)+\boldsymbol{\epsilon}^t] + c\left[(T-T_0) - T\ln\left(\frac{T}{T_0}\right)\right] - s_0 T + u_0 + \frac{1}{\rho}f(\xi), \quad (1)$$

where, $\mathbb{S}$, $\boldsymbol{\alpha}$, c, ρ, s_0 and u_0 are the effective compliance tensor, effective thermal expansion coefficient tensor, effective specific heat, mass density, effective specific entropy, and effective specific internal energy at the reference state, respectively. The symbols $\boldsymbol{\sigma}$, T, T_0, $\boldsymbol{\epsilon}^t$ and ξ denote the Cauchy stress tensor, temperature, reference temperature, transformation strain, and martensitic volume fraction, respectively.

Based on Saint–Venant's solution for torsion of prismatic bars with general cross sections (Higgins, 1942), it is known that in pure torsion of prismatic bars with circular cross section the no warpage assumption is valid (Sokolnikoff, 1956). In this special case, the state of stress and strain is one dimensional and shear strain varies linearly from the central axis toward the outer radius. The one-dimensional reduced stress, strain, and transformation strain tensors have the following forms:

$$\boldsymbol{\sigma} = \begin{bmatrix} 0 & 0 & 0 \\ 0 & 0 & \tau_{\theta z} \\ 0 & \tau_{\theta z} & 0 \end{bmatrix}, \quad \boldsymbol{\epsilon} = \begin{bmatrix} 0 & 0 & 0 \\ 0 & 0 & \epsilon_{\theta z} \\ 0 & \epsilon_{\theta z} & 0 \end{bmatrix}, \quad \boldsymbol{\epsilon}^t = \begin{bmatrix} 0 & 0 & 0 \\ 0 & 0 & \epsilon^t_{\theta z} \\ 0 & \epsilon^t_{\theta z} & 0 \end{bmatrix}, \quad (2)$$

where $\tau_{\theta z}$, $\epsilon_{\theta z}$ and $\epsilon^t_{\theta z}$ are the shear stress, shear strain, and transformation shear strains, respectively.

All the effective material properties in (1) are assumed to vary with the martensitic volume fraction (ξ) as

$$\mathbb{S} = \mathbb{S}^A + \xi\Delta\mathbb{S}, \quad \boldsymbol{\alpha} = \boldsymbol{\alpha}^A + \xi\Delta\boldsymbol{\alpha}, \quad c = c^A + \xi\Delta c,$$
$$s_0 = s_0^A + \xi\Delta s, \quad u_0 = u_0^A + \xi\Delta u_0, \quad (3)$$

where the superscripts A and M represent the austenite and martensite phases, respectively. The symbol $\Delta(\cdot)$ denotes the difference of a quality $(\cdot)$ between the martensitic and austenitic phases, i.e. $\Delta(\cdot) = (\cdot)^M - (\cdot)^A$. In (1), $f(\xi)$ is a hardening function that models the transformation strain hardening in the SMA material. In the Boyd–Lagoudas polynomial hardening model (Lagoudas, 2008), this function is given by

$$f(\xi) = \begin{cases} \frac{1}{2}\rho b^M \xi^2 + (\mu_1+\mu_2)\xi, & \dot{\xi} > 0, \\ \frac{1}{2}\rho b^A \xi^2 + (\mu_1-\mu_2)\xi, & \dot{\xi} < 0, \end{cases} \quad (4)$$

where, ρb^A, ρb^M, μ_1 and μ_2 are material constants for transformation strain hardening. The first condition in (4) represents the forward phase transformation ($A \to M$) and the second condition represents the reverse phase transformation ($M \to A$). The constitutive relation of a shape memory material can be obtained by using the total Gibbs free energy as

$$\boldsymbol{\epsilon} = -\rho\frac{\partial G}{\partial \boldsymbol{\sigma}} = \mathbb{S}:\boldsymbol{\sigma} + \boldsymbol{\alpha}(T-T_0) + \boldsymbol{\epsilon}^t, \quad (5)$$

where $\boldsymbol{\epsilon}$ is the strain tensor (the one-dimensional form of strain corresponding to pure torsion is given in (2)). Considering the fact that any change in the state of the system is only possible by a change in the internal state variable ξ (Bo and Lagoudas, 1999), the evolution of the transformation strain tensor is related to the evolution of the martensitic volume fraction as $\dot{\boldsymbol{\epsilon}}^t = \boldsymbol{\Gamma}\dot{\xi}$, where $\boldsymbol{\Gamma}$ represents a transformation tensor related to the deviatoric stress tensor and determines the flow direction as

$$\boldsymbol{\Gamma} = \begin{cases} \frac{3}{2}\frac{H}{\bar{\sigma}}\boldsymbol{\sigma}', & \dot{\xi} > 0, \\ \frac{H}{\bar{\epsilon}^{tr}}\boldsymbol{\epsilon}^{tr}, & \dot{\xi} < 0. \end{cases} \quad (6)$$

In (6), H is the maximum uniaxial transformation strain and $\boldsymbol{\epsilon}^{tr}$ represents the transformation strain at the reverse phase transformation. The terms $\boldsymbol{\sigma}'$, $\bar{\sigma}$ and $\bar{\epsilon}^{tr}$ are the deviatoric stress tensor, the second deviatoric stress invariant and the second deviatoric transformation strain invariant, respectively, and are expressed as

$$\boldsymbol{\sigma}' = \boldsymbol{\sigma} - \frac{1}{3}(\mathrm{tr}\boldsymbol{\sigma})\mathbf{I}, \quad \bar{\sigma} = \sqrt{\frac{3}{2}\boldsymbol{\sigma}':\boldsymbol{\sigma}'}, \quad \bar{\epsilon}^{tr} = \sqrt{\frac{2}{3}\boldsymbol{\epsilon}^{tr}:\boldsymbol{\epsilon}^{tr}}, \quad (7)$$

where $\mathbf{I}$ is the identity tensor. Using the one-dimensional stress and strain state for pure torsion presented in (2), $\mathrm{tr}\boldsymbol{\sigma} = 0$ and the deviatoric stress tensor will be the same as the stress tensor, $\boldsymbol{\sigma}' = \boldsymbol{\sigma}$. The second deviatoric stress and transformation strain invariants are reduced to read:

$$\bar{\sigma} = \sqrt{3}|\tau_{\theta z}|, \quad \bar{\epsilon}^{tr} = \frac{2}{\sqrt{3}}|\epsilon^{tr}_{\theta z}|. \quad (8)$$

The transformation tensors for pure torsion are expressed as:

$$\boldsymbol{\Gamma}^+ = \frac{\sqrt{3}}{2}H\,\mathrm{sgn}(\tau_{\theta z})\begin{bmatrix} 0 & 0 & 0 \\ 0 & 0 & 1 \\ 0 & 1 & 0 \end{bmatrix}, \quad \boldsymbol{\Gamma}^- = \frac{\sqrt{3}}{2}H\,\mathrm{sgn}(\epsilon^{tr}_{\theta z})\begin{bmatrix} 0 & 0 & 0 \\ 0 & 0 & 1 \\ 0 & 1 & 0 \end{bmatrix}, \quad (9)$$

where sgn $(\cdot)$ is the sign function and the superscripts + and − for $\boldsymbol{\Gamma}$ represent the forward and inverse phase transformations, respectively.

An additional constraint on the material behavior is obtained by using the Second Law of Thermodynamics in the form of non-negativeness of the rate of entropy production density (Qidwai and Lagoudas, 2000a):

$$\boldsymbol{\sigma}:\dot{\boldsymbol{\epsilon}}^t - \rho\frac{\partial G}{\partial \xi}\dot{\xi} = \pi\dot{\xi} \geqslant 0, \quad (10)$$

where π is a thermodynamic force and can be obtained by substituting (1) and the evolution relation into (10) as

$$\pi = \boldsymbol{\sigma}:\boldsymbol{\Gamma} + \frac{1}{2}\boldsymbol{\sigma}:\Delta\mathbb{S}:\boldsymbol{\sigma} + \Delta\boldsymbol{\alpha}:\boldsymbol{\sigma}(T-T_0) - \rho\Delta c\left[(T-T_0) - T\ln\left(\frac{T}{T_0}\right)\right] + \rho\Delta s_0 T - \frac{\partial f}{\partial \xi} - \rho\Delta u_0. \quad (11)$$

Now, the transformation function that controls the onset of direct and reverse phase transformation is defined as

$$\Phi = \begin{cases} \pi - Y, & \dot{\xi} > 0, \\ -\pi - Y, & \dot{\xi} < 0, \end{cases} \quad (12)$$

where Y is a measure of internal dissipation due to microstructural changes during phase transformation. The transformation function represents the elastic domain in the stress–temperature state. In other words, when $\Phi < 0$ the material response is elastic and the martensitic volume fraction does not change $\left(\dot{\xi} = 0\right)$. During the forward phase transformation from austenite to martensite $\left(\dot{\xi} > 0\right)$ and the reverse phase transformation from martensite to austenite $\left(\dot{\xi} < 0\right)$, the state of stress, temperature and martensitic volume fraction should remain on the transformation surface, which is characterized by $\Phi = 0$. It can be seen that transformation surface in the stress–temperature space is represented by two

separate surfaces that are defined by $\xi = 0$ and $\xi = 1$. Any state of stress–temperature inside the inner surface ($\xi = 0$) represents the austenite state with an elastic response. Outside the surface $\xi = 1$, the material is fully martensite and behaves elastically. For any state of stress–temperature on or in between these two surfaces the material behavior is inelastic and a forward transformation occurs. A similar transformation surface exists for the reverse phase transformation.

In the one-dimensional case corresponding to pure torsion, substituting (9) into (11) and (12) and using the following relation between the constitutive model parameters:

$$\rho\Delta u_0+\mu_1=\frac{1}{2}\rho\Delta s_0(M_s+A_f),\ \ \rho b^A=-\rho\Delta s_0(A_f-A_s),$$
$$\rho b^M=-\rho\Delta s_0(M_s-M_f),$$
$$Y=-\frac{1}{2}\rho\Delta s_0(A_f-M_s)-\mu_2,\ \ \mu_2=\frac{1}{4}(\rho b^A-\rho b^M),\ \ \frac{d\sigma}{dT}=-\frac{\rho\Delta s_0}{H}, \quad (13)$$

the following explicit expressions for the martensitic volume fraction in direct and inverse phase transformation are obtained as

$$\xi^+=\frac{1}{\rho b^M}\left\{\sqrt{3}H|\tau_{\theta z}|+2\tau_{\theta z}^2\Delta S_{44}+f^+(T)\right\}, \quad (14)$$

$$\xi^-=\frac{1}{\rho b^A}\left\{\sqrt{3}H\tau_{\theta z}\mathrm{sgn}(\epsilon_{\theta z}^{tr})+2\tau_{\theta z}^2\Delta S_{44}+f^-(T)\right\}, \quad (15)$$

where

$$f^+(T)=\rho\Delta c\left[(T-T_0)-T\ln\left(\frac{T}{T_0}\right)\right]+\rho\Delta s_0(T-M_s), \quad (16)$$

$$f^-(T)=\rho\Delta c\left[(T-T_0)-T\ln\left(\frac{T}{T_0}\right)\right]+\rho\Delta s_0(T-A_f). \quad (17)$$

The parameters M_s and A_f are the martensitic start and austenite finish temperatures, respectively. By substituting the explicit expression of the martensitic volume fraction in the evolution equation and after integrating from zero to an arbitrary time, the transformation shear strain can be calculated. The constitutive relation (5) is now reduced to read:

$$\epsilon_{\theta z}=\frac{1+\nu}{E_A+\xi^{\pm}(E_M-E_A)}\tau_{\theta z}+\frac{1}{\rho b^{\pm}}\left\{\frac{3}{2}H^2\tau_{\theta z}+\sqrt{3}H\tau_{\theta z}^2\aleph^{\pm}\Delta S_{44}+\frac{\sqrt{3}}{2}H\aleph^{\pm}f^{\pm}(T)\right\}, \quad (18)$$

where ν is Poisson's ratio and is assumed to be the same for both phases. The + and − symbols are used for the direct and reverse phase transformations, respectively, and the other parameters are: $\aleph^+=\mathrm{sgn}(\tau_{\theta z}), \aleph^-=\mathrm{sgn}(\epsilon_{\theta z}^{tr}), \rho b^+=\rho b^M$, and $\rho b^-=\rho b^A$.

3. Analytical study of SMA helical springs

In this section, we present two different analytical methods for calculating the loading–unloading response of SMA helical springs under axial loads. For helical springs with a large spring index (defined as $m = R_m/R$, where R_m is the mean coil radius and R is the cross section radius) and a small helix angle, both the curvature and pitch effects can be ignored without losing much accuracy.[1] In this special case, the pure torsion analysis of a straight bar can be used for analyzing the helical springs. For most practical springs, the pitch angle is smaller than 15°, but the spring index varies in a wide range. The curvature correction is added to the theory used for studying the pure torsion of a straight bar and a more precise solution is obtained for analyzing SMA helical springs with smaller spring indices.

3.1. Analysis based on exact solution for pure torsion of SMA bars

We presented an exact solution for pure torsion of SMA straight bars with circular cross section in our previous work (Mirzaeifar et al., 2010). This solution is used here for analyzing the SMA helical springs and it is denoted by SBTM (straight bar torsion model) throughout the text. Considering a straight bar with a general cross section in the xy plane (z is along the bar axis), the state of shear strain at a point in the cross section is, $\gamma_{zx}=2\epsilon_{zx}=\theta\left(\frac{\partial\psi}{\partial x}-y\right)$ and $\gamma_{zy}=2\epsilon_{zy}=\theta\left(\frac{\partial\psi}{\partial y}+x\right)$, where θ is the twist angle per unit length and ψ represents the warping function representing the cross sectional deformation along the z-axis. For circular (Sokolnikoff, 1956) and some other special cross sections (Chen, 2004), the warpage is zero and the shear strains distribute linearly through the thickness. For a bar with a circular cross section, the shear strain in (18) can be related to twist angle per unit length as $\epsilon_{\theta z}=\frac{1}{2}r\theta$, where r is the distance from the axis of the bar. Substituting (14) or (15) into (18) and considering the special case in which both the shear stress and the shear transformation strains are positive, (18) can be rewritten as:

$$\tau_{\theta z}^4+F_1\tau_{\theta z}^3+\left(F_2+F_2^*r\theta\right)\tau_{\theta z}^2+\left(F_3+F_3^*r\theta\right)\tau_{\theta z}+\left(F_4+F_4^*r\theta\right)=0 \quad (19)$$

with the coefficients given in Appendix A. This relation is a quartic equation that can be solved analytically using Ferrari's method (Cardano et al., 2007) for finding the shear stress $\tau_{\theta z}$ as a function of twist angle and distance from z-axis as:

$$\tau_{\theta z}=\wp^{\pm}(r,\theta), \quad (20)$$

which is given explicitly in Appendix A. For an SMA bar under torsion (with the axis of bar along z-direction), in the most general case the cross section may be divided into three regions (see Mirzaeifar et al., 2010, for more details). In the inner region, the material is in the austenite phase and the relation $\tau_{\theta z}=G_A r\theta$ with $G_A=\frac{E_A}{2(1+\nu)}$ holds. In the middle region, the phase transformation has started ($0<\xi<1$) and the relation $\tau_{\theta z}=\wp^+(r,\theta)$ expressed in (20) is valid. In the outer region the phase transformation is completed and the material is in the martensite phase. In this region stress is calculated as $\tau_{\theta z}=\tau_{\theta z}^f+G_M r(\theta-\theta^f)$, where $\tau_{\theta z}^f$ and θ^f are the shear stress and the twist angle at which the phase transformation has been completed ($\xi=1$) everywhere. For a bar in the austenite phase with $\theta=0$, by increasing the twist angle, the phase transformation starts from the outer radius and spreads toward the center. With more increase of the twist angle, the third region with fully transformed martensite spreads from the outer radius toward the center. The outer radius of the inner and middle regions are denoted by r_1 and r_2 in the sequel. During the loading phase, in any cross section the resultant torque is given by

$$\mathbb{T}^+=2\pi\int_0^{r_1}G_A\theta r^3dr+2\pi\int_{r_1}^{r_2}\wp^+(r,\theta)r^2dr+2\pi\int_{r_2}^{R}\left(\tau_{\theta z}^f+G_M r(\theta-\theta^f)\right)r^2dr. \quad (21)$$

In unloading, the cross section is divided into three regions as well. The material in the inner region is in the austenite phase and has experienced both elastic loading and unloading (the outer radius of this region is denoted by r_1^*). In the middle region the bar has experienced phase transformation during loading but the unloading was elastic (the outer radius of this region is denoted by r_2^*). The martensitic volume fraction for any material point in this region is unchanged during unloading. The outer region of the cross

[1] It is known that for helical springs with $m > 4$ and a pitch angle smaller than 15°, the error of using SBTM for analyzing helical spring leads to less than 2% error with common engineering materials used in practical springs (see Ancker and Goodier, 1958a; Wahl, 1944, for more details).

section of a bar during unloading in torsion contains the material that has experienced phase transformation during both loading and unloading phases. A detailed analysis is presented by the authors in a previous work (Mirzaeifar et al., 2010). During unloading, the torque in the cross section is given by

$$\mathbb{T}^- = 2\pi \int_0^{r_1^*} G_A \theta r^3 dr + 2\pi \int_{r_1^*}^{r_2^*} \left(\tau_{\theta z}^{\ell} - G_{eff} r \Delta\theta\right) r^2 dr + 2\pi \int_{r_2^*}^{R} \wp^-(r,\theta) r^2 dr, \tag{22}$$

where the parameter $\tau_{\theta z}^{\ell}$ represents the value of shear stress for any point at the end of the loading phase and $\Delta\theta$ is the amount of reverse twist angle during unloading (Mirzaeifar et al., 2010).

Since in this assumption the spring is considered as a straight bar of length $l = 2\pi N R_m$, where N is the number of active coils, the total angular deflection of one end of the bar with respect to the other end is given by $\Theta = 2\pi N R_m \theta$. Because the effective moment arm of the axial load F is equal to R_m, the deflection of the spring at the end point is given by

$$\delta = \Theta R_m = 2\pi N R_m^2 \theta. \tag{23}$$

For any deflection of the spring ends (23) is used for finding the twist angle per unit length θ. Substituting this value in (20), the shear stress distribution in the cross section is calculated. Having the shear stress distribution, the resultant torque in the cross section is obtained by (21) or (22) and the axial force corresponding to the assumed end displacement is calculated by dividing the torque by the coil mean radius: $F = \mathbb{T}^{\pm}/R_m$. In this approximation, the effect of direct shear force on the cross section is ignored along with the curvature and pitch effects. In the following section, a curvature correction is added to the analysis and in each cross section both the torque and direct shear forces are taken into consideration.

3.2. Curvature correction

Although the analysis of helical springs based on SBTM is of enough accuracy for most practical helical springs, there have been many efforts in the literature for improving this theory (Wahl, 1944; Ancker and Goodier, 1958a,b,c). It is known that due to the curvature effect, the shear stress distribution in the cross section is not axisymmetric. In this section, a curvature correction is implemented in the solution presented in the previous section. The solution of this section is applicable to SMA helical springs with large spring indices but small pitch angles. This includes nearly all the practical helical springs (Wahl, 1944). This solution method is denoted by CBTM (curved bar torsion model) throughout the text.

First, we consider the pure torsion of an SMA curved bar. A slice of such a bar is shown in Fig. 1. Applying a torque the two faces of this cross section will rotate with respect to each other by an angle $d\beta$. Since the initial length of the filament passing through the points a and b are not the same, the strain distribution in the cross section is not axisymmetric. This will result in a non axisymmetric stress distribution with a larger value for the material points near the axis AB. The non axisymmetric shear stress distribution in the cross section can be decomposed into an axial component τ_a and a transverse component τ_t as shown in Fig. 1. If we assume that the cross section is rotating about an axis passing through the center o (at the center of rotation, the shear stress is zero), and considering the fact that the shear stress at b is larger than the stress at a, such a distribution cannot be in equilibrium; there will be a torque in the cross section (Wahl, 1944). So, it can be concluded that for a curved bar under torsion, the zero shear stress point or the center of rotation does not coincide with the cross section center.

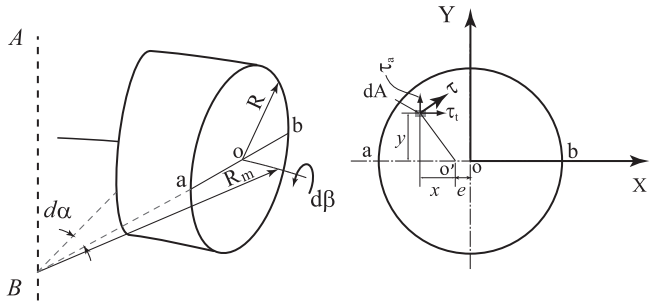

Fig. 1. Torsion of a curved bar.

Considering the symmetry conditions in the cross section, the forces caused by the transverse shear stress component τ_t are in equilibrium when the rotation center is anywhere on the axis ab. The rotation center o' is shown in Fig. 1. The distance e is found by the method presented in the sequel.

In the coordinate system xy with the origin o', when the slice sides rotate by the amount $d\beta$ with respect to each other the relative movement of the ends of any filament corresponding to dA in Fig. 1 is $\sqrt{x^2+y^2}\,d\beta$. Considering the fact that the length of this filament in the undeformed configuration is $(R_m - e - x)d\alpha$, the shear strain corresponding to this point in the cross section is

$$\gamma = \frac{\sqrt{x^2+y^2}}{R_m - e - x}\frac{d\beta}{d\alpha}, \tag{24}$$

where the shear strain γ is along the direction of τ in Fig. 1. The geometrical parameters in (24) are shown in Fig. 1. Now, the expression given for the shear strain in (24) should replace the expression $r\theta$ (that is the strain in the straight bar case) in (19) and all the coefficients given in Appendix A. The new quartic equation obtained by this substitution is solved to find an explicit expression for the shear stress in the regions with phase transformation. We denote the shear stress in this case by $\tau = \hat{\wp}^{\pm}(x,y,e,d\beta/d\alpha)$, where the explicit expression for shear stress is similar to that given in Appendix A by replacing the parameter $r\theta$ with the shear strain of a curved bar in (24). For a curved bar under pure torsion, the resultant force in the cross section should be zero. Due to symmetry of the transverse shear stress about the axis ab, the forces caused by this stress component are in static equilibrium. The static equilibrium for the forces caused by the axial component of the shear stress is expressed by

$$\int_A \tau_a dA = \int_{A_1} \frac{G_A x}{R_m - e - x}\frac{d\beta}{d\alpha} dA_1 + \int_{A_2} \hat{\wp}^{\pm}(x,y,e,d\beta/d\alpha)\frac{x}{\sqrt{x^2+y^2}} dA_2 + \int_{A_3} \left(\tau_a^f + \frac{G_M x}{R_m - e - x}\frac{d\beta - d\beta^f}{d\alpha}\right) dA_3 = 0, \tag{25}$$

where A_1 is that portion of the section that has not experienced the phase transformation. The portion of the cross section with phase transformation is denoted by A_2 and the parts in which the phase transformation has been completed by A_3. For each material point with completed phase transformation ($\xi = 1$), the parameter τ_a^f is the the axial component of shear stress corresponding to $d\beta^f$ that is the twist angle of phase transformation completion for that material point. Now, the only unknown parameter in (25) is the position of the rotation center e. In contrast with the elastic torsion of a bar, in the case of an SMA curved bar the second and third integrals in (25) cannot be calculated analytically. We use trapezoidal numerical integration method. In our numerical examples, we well

compare the results of the present model with those of a three-dimensional finite element simulation.

For analyzing SMA helical springs based on the pure torsion of an SMA curved bar, a minor correction is needed to take into account the direct shear force in the cross section. In an SMA helical spring a direct shear force F and a torque $R_m F$ are acting in each cross section. The equilibrium equations in the cross section in this case read

$$\int_A \tau_a dA = F \quad \text{and} \quad \int_A \tau_a x dA + \int_A \tau_t y dA = R_m F, \tag{26}$$

where in the most general case, the cross section is divided into three regions similar to the previous cases. For analyzing the SMA spring using the curved bar theory, a predefined displacement is considered for the spring ends. The total rotation of the spring ends with respect to each other is calculated by $\widehat{\Theta} = \delta / R_m$. The twist angle per curvature angle is given by

$$\frac{d\beta}{d\alpha} = \frac{\delta}{2\pi R_m N}. \tag{27}$$

The expression in Appendix A (by replacing $r\theta$ with the shear strain of a curved bar in (24)) is used to calculate the shear stress. Since the axial force F is unknown, in contrast with the pure torsion case the parameter e cannot be obtained directly by solving (26). Hence, first an initial value[2] is considered for e. Using this value the axial force F is calculated using both expressions in (26). A trial and error method is then used to find the value of e for which the difference of the axial forces calculated from the two conditions in (26) is smaller than a tolerance (1N in the numerical examples of this paper).

4. Helical SMA spring test

An SMA helical spring shown in Fig. 2 is used for obtaining the experimental results. The spring has a mean coil radius of R_m = 2.1 cm, an initial length of 12.98 cm and the cross section radius of 6.25 mm (Speicher et al., 2009). The helical spring is placed in a cylindrical shape tension/compression device and a 250 kN MTS Universal Testing Machine is used for compressing the spring. The tension/compression device is a cylindrical-shaped damper that provides the ability to test a variety of SMA elements (Speicher et al., 2009). The body and the shaft of the device are made out of standard 304 stainless steel cylinders. The nitinol helical spring is loaded on the center shaft using a nut. The outer cylinder covers both the spring and the center shaft. The spring ends are free to rotate during loading and unloading (see (Speicher et al., 2009) for pictures of the test device). The quasi-static loading rate is set to 0.127 cm/s. Using this loading rate, the temperature change due to the latent heat is negligible and the test can be considered isothermal. Compression tests are done in the ambient temperature of 27 °C. The experimental set-up and the test procedure are explained in detail in Speicher et al. (2009). This reference contains a comprehensive study of three different SMA devices for applications as bracing elements in buildings.

The spring is made from Nitinol Alloy 508 (50.8% at.% Nickel). A simple tension test is carried out on a bar of the same alloy and a stabilized loading–unloading cycle for this specimen is shown in Fig. 3(a). Due to the thermal and mechanical treatments done on the initial SMA stock for producing a helical spring, the material properties for the spring may have a slight difference with the properties of SMA stock. The properties of Material II given in Table 1 are calibrated by comparing the results of analytical and numerical analyses with the experimental results of Speicher et al. (2009) done on the SMA helical spring and the simple tension test in Fig. 3(a). The response of material with calibrated properties in simple tension is compared with the experimental results in Fig. 3(a). In order to take the uncertainty effect in calculating the material properties into consideration, we will present a discussion on the effect of changing material properties on the spring response in the sequel.

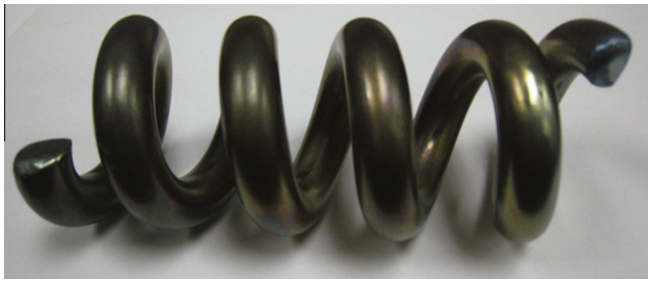

Fig. 2. The SMA helical spring used in the experimental study.

5. Finite element simulation of SMA helical springs

For analyzing SMA helical springs using the finite element method, the three-dimensional constitutive relations of Section 2 are used and an appropriate user subroutine (UMAT) is written by FORTRAN in the commercially available finite element program ABAQUS that enables this code to model SMA structures using solid elements and some two-dimensional elements. The details of implementing the constitutive equation in a displacement based finite element formulation is given in Qidwai and Lagoudas (2000b) and many case studies for validating the model are presented in Mirzaeifar et al. (2009), Mirzaeifar et al. (2010) and Mirzaeifar et al. (in press). In the present study, for comparison purposes the spring is modeled three dimensionally (in contrast with some finite element models in the literature that use beam elements for modeling the SMA helical springs, e.g. Toi et al., 2004). Three dimensional quadratic brick elements with reduced integration (element C3D20R in ABAQUS) are used in the finite element model of the helical spring. A convergence analysis is performed for choosing the appropriate number of elements by considering the shear stress distribution in the cross section and the load–displacement response as the convergence criteria. The stress distribution is considered to be converged when the maximum difference is smaller than 0.1 MPa and the convergence criterion of the maximum difference for the load–displacement response is 10 N. We observe that the convergence is achieved by using 7500 elements. All the finite element simulations are done using this mesh. A schematic of the finite element mesh is shown in Fig. 4.

For simulating the spring in compression, two rigid surfaces in contact with the spring ends are considered (see Fig. 4). The lower rigid surface is constrained in all directions and a time varying boundary condition is defined for the upper surface for modeling compression. A node to surface contact with a friction coefficient of 0.1 is defined between the solid elements at the end rings and the shell elements in the upper and lower rigid surfaces. The supporting shaft in the experiments is modeled with a cylindrical rigid surface inside the helical spring with a diameter slightly (0.2 mm) smaller than the inner radius of the coil (this shaft is shown in Fig. 4 (left) but not in Fig. 4 (right) to show the spring more clearly). For avoiding high local stresses and the convergence problems in

[2] The loading/unloading response of the SMA spring is analyzed by applying the total axial deflection incrementally. In the first few increments the entire cross section is in the austenite phase and hence the location of the rotation center is calculated easily as the shear stress expression in (26) is integrable. For the subsequent load increments, the initial guess for the parameter e for each increment is the value obtained in the previous increment.

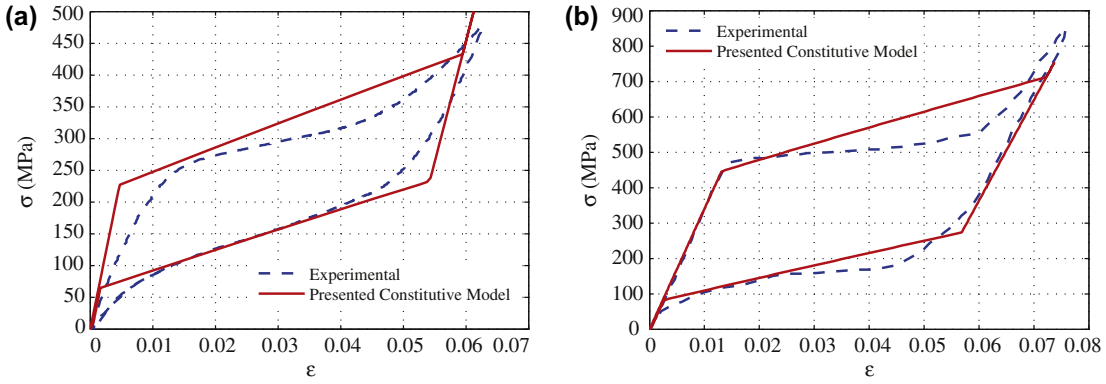

Fig. 3. The calibrated material properties versus experiments in simple tension test for the material used in (a) Speicher et al. (2009), and (b) Toi et al. (2004) tests on SMA helical springs.

Table 1
SMA material parameters.

Material constants	A generic SMA (Material I) (Qidwai and Lagoudas, 2000b)	$Ni_{50.8}Ti_{49.2}$ (Material II) (Speicher et al., 2009)	Material III (Toi et al., 2004)
E^A	70.0×10^9 Pa	48.5×10^9 Pa	34×10^9 Pa
E^M	30.0×10^9 Pa	38.2×10^9 Pa	28.5×10^9 Pa
$\nu^A = \nu^M$	0.3	0.42	0.33
α^A	22.0×10^{-6}/K	–	–
α^M	10.0×10^{-6}/K	–	–
$\rho\Delta c = c^M - c^A$	0.0 J/(m^3 K)	0.0 J/(m^3 K)	0.0 J/(m^3 K)
H	0.05	0.047	0.047
$\frac{d\sigma}{dT}$	7.0×10^6 Pa/K	6.0×10^6 Pa/K	9.8×10^6 Pa/K
A_f	315.0 K	288.15 K	292.6 K
A_s	295.0 K	258.15 K	273.7 K
M_s	291.0 K	258.15 K	252.9 K
M_f	271.0 K	218.15 K	220.8 K

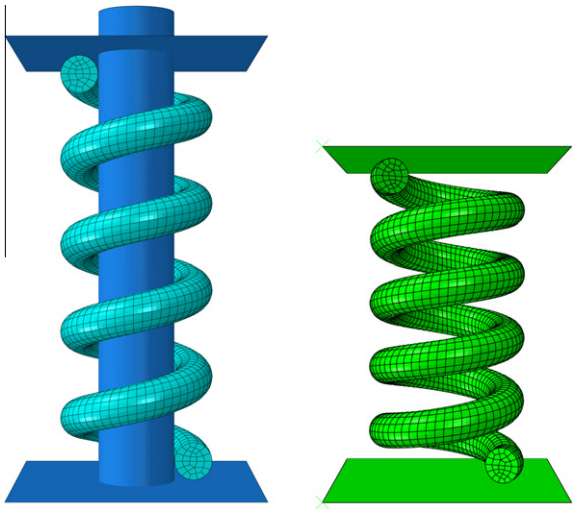

Fig. 4. Finite element model of the SMA spring in the initial (left) and compressed (right) configurations.

the finite element solution, the contact between the solid elements of the spring and the rigid cylindrical surface is considered frictionless. Both spring ends are free to rotate in the numerical simulation. The automatic time increment option in ABAQUS is used with an initial guess of dividing the loading and unloading steps into 100 increments and the non-linear geometry option is activated. The geometry of the spring modeled in the finite element simulation is exactly the same as the helical spring in the experimental tests (see Section 4).

6. Numerical results

In this section, several case studies are presented for demonstrating the efficiency of the proposed analytical solution for analyzing SMA helical springs. The accuracy of the proposed exact solution for pure torsion of SMA bars with circular cross section was studied in Mirzaeifar et al. (2010). As mentioned in Section 5, the developed finite element code for analyzing SMA structures was verified in several case studies in the previous works of the authors (Mirzaeifar et al., 2009; Mirzaeifar et al., 2010; Mirzaeifar et al., in press). In the sequel, the accuracy of the proposed model for analyzing SMA carved bars is studied by comparing the results of this model with those of finite element simulations. Then, an SMA helical spring is considered and the results obtained based on the straight bar torsion, curved bar torsion, and finite element simulations are compared. A case study is presented for comparing the analytical and numerical results against the experimental results as well. The effect of changing material properties and temperature on the response of SMA helical spring subjected to axial loading–unloading cycle is studied and some practical recommendations are given for improving the behavior of SMA helical springs used for damping and dissipating energy in recentering devices in buildings subjected to external loads, especially during seismic events.

6.1. Verification of the curved SMA bar torsion

In order to verify the proposed solution for the SMA curved bar torsion problem, a case study is considered and the analytical results are compared with the finite element simulation outputs. Consider an SMA curved bar with $R_m = 2$ cm, the cross section radius $R = 6$ mm, and angle $\alpha = 20°$ (see Fig. 1). For verification purposes, the material properties of a generic SMA as reported previously in the literature (Qidwai and Lagoudas, 2000b) are used. These properties are given in Table 1 as Material I. The left end of the bar is constrained and a twist angle of 0.04 rad is applied to the right end. The bar is considered to be in the austenite finish temperature, $T = 315$ K.

The finite element model of the SMA curved bar is shown in Fig. 5(a). The details of modeling this bar in the finite element code ABAQUS are explained in Section 5. The martensitic volume fraction distribution in the cross section of this bar is shown in

Fig. 5(b). It is seen that in contrast with the straight bar torsion (Mirzaeifar et al., 2010), in the case of a curved bar, the martensitic volume fraction distribution is not axisymmetric as the zero stress point o' does not coincide with the cross section center.

Distribution of the axial component of shear stress τ_a along the diameter ab (see Fig. 1) calculated by our method and the finite element simulation is shown in Fig. 6. The shear stress is plotted along this diameter in the coordinate system XY with the origin at o (see Fig. 1). The zero shear stress occurs at a point with a distance $e = 0.1$ mm from the center of the cross section. Although e is very small, it has a significant effect on the stress and martensitic volume fraction distributions in the cross section. The non symmetry of the shear stress distribution is clearly seen in Fig. 6 ($\tau_a = 120.1$ MPa at point a and $\tau_a = 104.3$ MPa at point b).

The martensitic volume fraction distribution along the diameter ab is shown in Fig. 7. The curvature clearly affects the phase transformation and as it is shown the material points closer to the axis have higher volume fractions compared to the outer points. This non symmetry is seen in the finite element results as well (see Fig. 5(b)). As it is shown in Figs. 6 and 7, there is good agreement between the results of our method and the finite element simulation results.

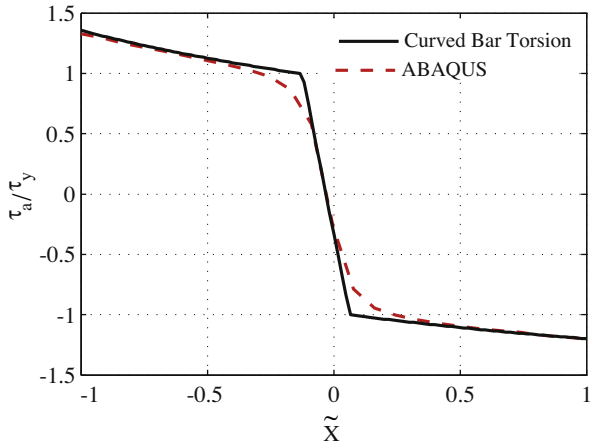

Fig. 6. Distribution of τ_a in an SMA curved bar subjected to torsion along diameter ab in Fig. 1 ($\tilde{X} = X/R$ and $\tau_y = 88.1$ MPa is the shear stress at the start of phase transformation obtained by solving (14) for $\xi^+ = 0$).

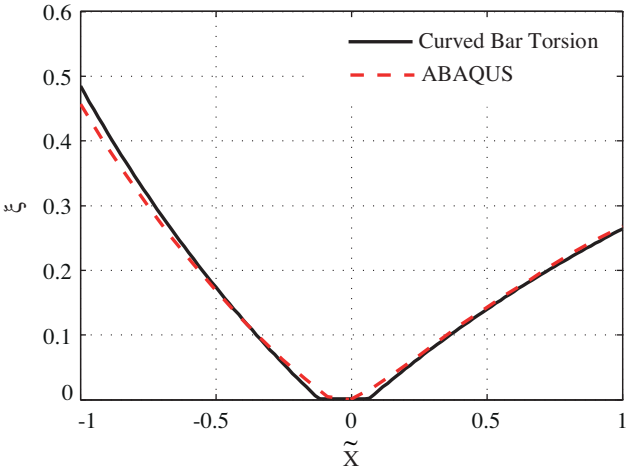

Fig. 7. Distribution of the martensitic volume fraction in an SMA curved bar subjected to torsion along diameter ab in Fig. 1 ($\tilde{X} = X/R$).

6.2. Analytical and numerical results for SMA helical springs

In this section, by considering a practical case study we will compare the results of our analytical formulation with the results of a finite element simulation. We consider an SMA helical spring with dimensions given in Section 4. Details of the finite element modeling are given in the previous section. The Nitinol Alloy 508 (50.8% at.% Nickel) material properties are considered for all the case studies. As explained in Section 4, these properties are calibrated from a simple tension test and the experimental tests on the SMA helical spring and are given in Table 1 as Material II. A loading–unloading cycle with maximum stroke of $\delta = 2.75$ cm is considered. The spring is at the ambient temperature $T = 27$ °C. A schematic of the undeformed spring in the finite element model is shown in Fig. 4(left). The finite element mesh at the end of loading cycle is shown in Fig. 4(right).

The load deflection plots in the loading–unloading cycle obtained based on SBTM, CBTM, and the finite element simulation are compared in Fig. 8. As it is shown in this figure, adding the curvature correction to the straight bar theory increases the agreement between the analytical and numerical results. The difference between the results of the curved bar theory and the numerical simulations perhaps is caused by ignoring bending due to the pitch effect in the analytical solution. However, considering the remarkable computational time reduction in using the analytical results reveals the value of analyzing the SMA helical springs using our proposed analytic solution. The finite element simulation takes almost 2 h on a 2 GHz CPU with 2 GB RAM while the analytic solution results based on the curved bar torsion are obtained in less than 2 min and the solution based on the straight bar torsion is obtained in a few seconds on the same system (the solution

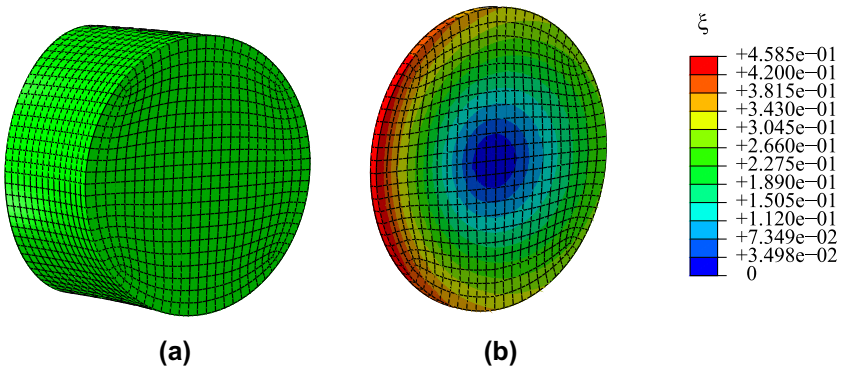

Fig. 5. (a) Finite element model for simulating torsion of an SMA curved bar, and (b) the non-axisymmetric distribution of martensitic volume fraction for the torsion of a curved bar.

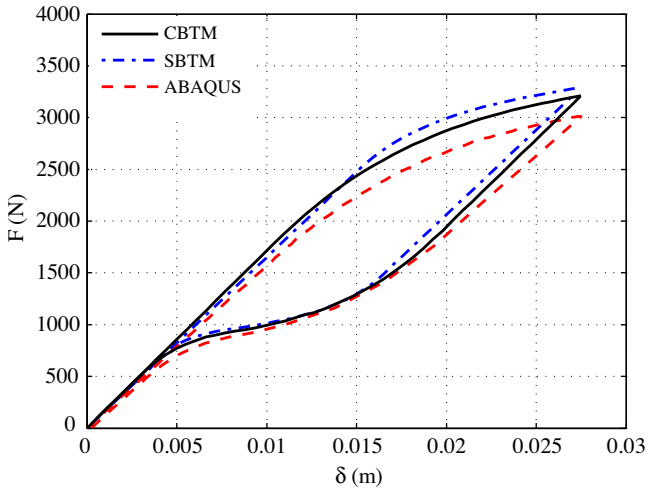

Fig. 8. Axial force versus axial displacement for an SMA helical spring calculated by the analytic solutions (CBTM: curved bar torsion model, STBM: straight bar torsion model) and the finite element simulation.

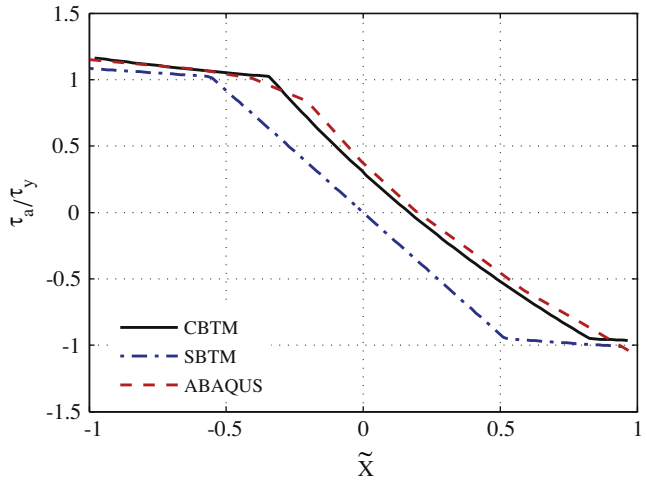

Fig. 9. Distribution of τ_a in the cross section of an SMA spring subjected to axial compression (along a diameter like ab in Fig. 1). CBTM: curved bar torsion model, STBM: straight bar torsion model, $\tilde{X} = X/R$ and τ_y = 138.2 MPa is the shear stress at the start of phase transformation obtained by solving (14) for $\xi^+ = 0$.

based on CBTM takes more time because the parameter e should be obtained iteratively as was explained in Section 3.2). The decrease in the computational time will be even more significant when repetitive simulations are needed, e.g. in most optimization procedures (Papadimitriou and Steiglitz, 1982; Goldberg, 1989).

The axial component of shear stress τ_a in the cross section on a horizontal diameter (like the diameter ab in Fig. 1) is calculated using SBTM, CBTM and finite element simulations[3] and the results are compared in Fig. 9. The martensitic volume fraction distributions obtained by these solution methods are depicted in Fig. 10. As it is shown in Figs. 9 and 10, unlike the load–displacement response, the stress and martensitic volume fraction distributions are highly affected by adding the curvature correction to SBTM. It is evident that CBTM predicts the stress and martensitic volume fraction distributions with a good agreement with the three-dimensional finite element simulations. As it is shown in Fig. 9, in contrast with the pure torsion of a curved bar, the zero shear stress point (the rotation center o') is located at a point toward the outer surface of the curved bar (compare the zero stress points in Figs. 6 and 9 and see the diameter ab in Fig. 1). This phenomenon is due to direct shear force in the cross section in formulating the SMA helical spring. Also, it is worth noting that, unlike the elastic curved bar torsion, in the SMA helical spring the zero shear stress point is not fixed in the cross section; it moves during loading and unloading. Fig. 11 shows the movement of the rotation center in the SMA helical spring cross section. It is seen that when the cross section is in the austenite phase and the spring response is elastic, the rotation center is fixed. When phase transformation occurs during loading and unloading, the zero shear stress point moves toward the outer surface of the curved bar and comes back to the elastic position.

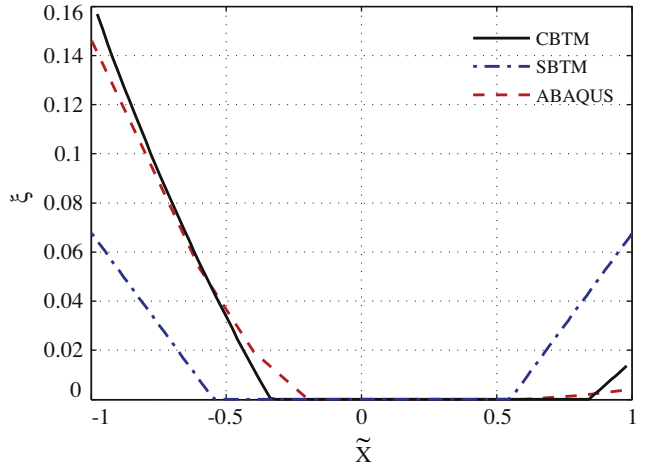

Fig. 10. Distribution of martensitic volume fraction in the cross section of an SMA spring subjected to axial compression (along a diameter like ab in Fig. 1). CBTM: curved bar torsion model, STBM: straight bar torsion model, $\tilde{X} = X/R$.

6.3. Experimental results

In this section, we use the experimental data of an SMA helical spring from a previous work of the second author (Speicher et al., 2009) for studying the accuracy of our analytical and numerical

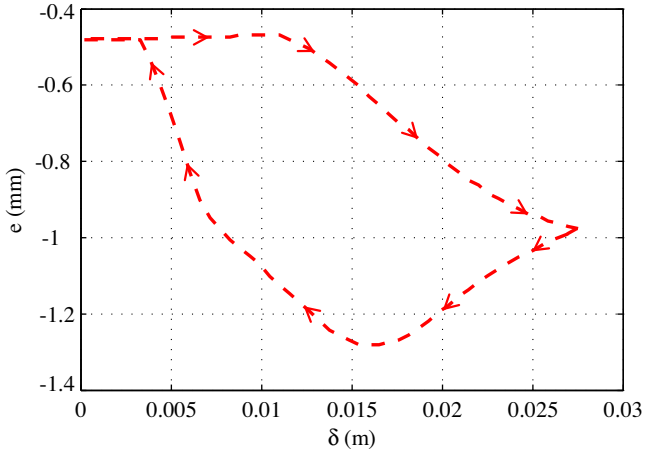

Fig. 11. The location of torsion centroid (o') in the cross section of the SMA helical spring during loading and unloading phases.

[3] In practice, when a helical spring is loaded between two planar plates (like the experimental test and the finite element simulation in the present paper), the applied end loads are eccentric with respect to the spring axis and hence the spring is subjected to a global bending. This global bending causes a lateral deflection with respect to the spring axis that is maximum at the middle of the spring. To avoid this global bending effect, the finite element results are reported for a cross section in the first upper ring of the spring (Wahl, 1944).

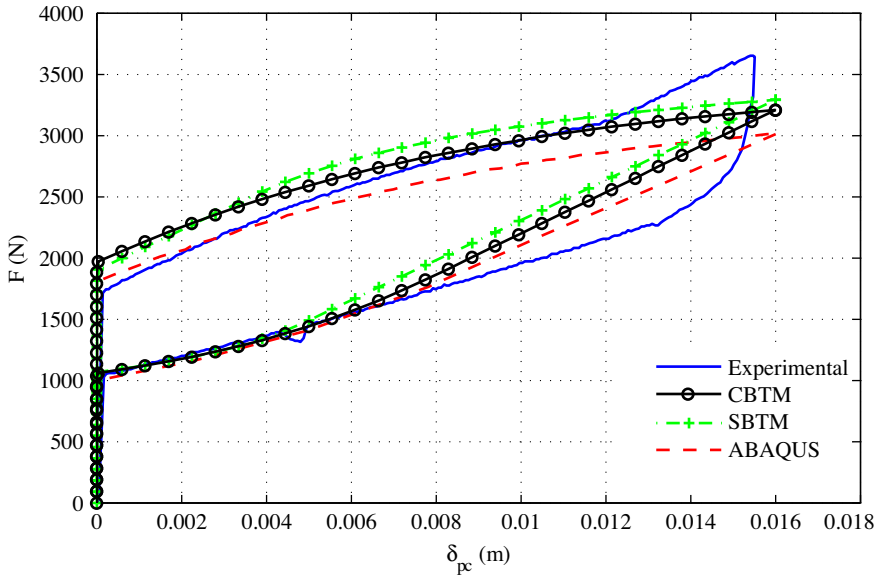

Fig. 12. Axial force versus axial displacement (considering the pre-compression) for an SMA helical spring calculated by the analytic solutions (CBTM: curved bar torsion model, STBM: straight bar torsion model), finite element simulations, and experimental tests.

models. In performing the experiments, a setup as explained in Section 4 is used. The SMA helical spring is placed in a tension/compression cylindrical device. In order to increase the initial stiffness of the device (that is preferred when the spring is used for energy dissipation in seismic events), a precompression of 1.15 cm is given to the spring by tightening a nut on the shaft that carries the spring (see Speicher et al., 2009, for more details on the experimental set-up). The spring is studied under various loading–unloading cycles. We will compare our analytical and numerical simulation results with those of an experiment in which the spring is compressed to δ_{pc} = 1.6 cm and then unloaded (δ_{pc} is the displacement of the ends of a precompressed spring). The results of loading–unloading cycle for this spring obtained by SBTM, CBTM, finite element simulation, and experimental results are compared in Fig. 12.

As it is shown in Fig. 12, due to the precompression effect the spring does not respond to the axial forces smaller than the precompression force. The presented analytical and numerical analysis predict the precompression force with less than 10% error compared to the experimental results. A good agreement is seen between the analytical, numerical, and experimental results during the loading–unloading phase. At the end of loading, a sudden jump occurs in the experimental load–deflection curve. This jump may be caused by a contact between the spring rings.[4] The contact at the end of the loading phase causes severe local stress concentration and local phase transformation at the contact points. The locally contact induced phase transformation may be an explanation for a slight disagreement that is seen between the analytical and experimental results at the beginning of the unloading phase.[5] However, all the results are in good agreement for the rest of the unloading phase.

Two other case studies are considered for validating the presented analytical formulation with the experimental results. Toi et al. (2004) presented experimental results for SMA helical springs in tension and compared them with their finite element simulation results. In the numerical simulations presented by Toi et al. (2004), an incremental finite element using linear Timoshenko beam elements is formulated using a total Lagrangian approach for the superelastic, large deformation analysis of SMA helical springs. A simple tension test is carried out on the material of springs as shown in Fig. 3(b). The presented constitutive model is calibrated using these results and the calibrated properties for this material are given in Table 1 as Material III. Fig. 3(b) compares the simulated response of material using the presented constitutive model with the experimental results for simple tension. Two different springs are considered in experiments. Both springs have a mean coil radius of R_m=3.65 mm, and the cross section radius of 0.5 mm. One of the springs has a total length of 5 mm and five turns and the other one has a total length of 10 mm with ten turns. Both springs are subjected to tension and tests are carried out at T = 305 K. The analytical results obtained by the present CBTM are compared with the experimental and numerical results of Toi et al. (2004) in Fig. 13. A good agreement is seen between the CBTM and the finite element simulation results using Timoshenko beam elements. Both the numerical and analytical results have a slight difference with the experiments. This difference is most likely caused by the non-linearity effects due to the extreme amount of elongation in the experiments.

6.4. Uncertainty in material properties

As mentioned earlier, making an SMA helical spring from a straight bar is done by performing a set of thermal and mechanical treatments on the initial SMA stock. Due to this complicated thermo-mechanical treatment, the material properties are not the same as the initial stock and in practice if a number of helical springs are made from an SMA stock, a slight difference may be seen in the material properties of these springs. Andrawes and DesRoches (2007) presented a detailed study of the effect of a change in the material properties of SMAs in uniaxial tension on the hysteretic response and energy dissipation capability of these

[4] As shown in Fig. 2 due to manufacturing difficulties, the helical spring does not have a perfectly uniform shape and the first and last rings have smaller pitch angles compared to the other rings. An initial contact occurs in these rings at the end of the loading phase.

[5] It is worth noting that in modeling the loading–unloading phase even in a simple uniaxial case, the constitutive equation used in this paper (the Boyd–Lagoudas' polynomial hardening model) shows a slight difference at the beginning of the unloading phase. Some improvements are provided for the hardening function to reduce this difference (see Chapter 3 in Lagoudas (2008)). As we are seeking closed-form solutions in this paper, the polynomial hardening function is preferred.

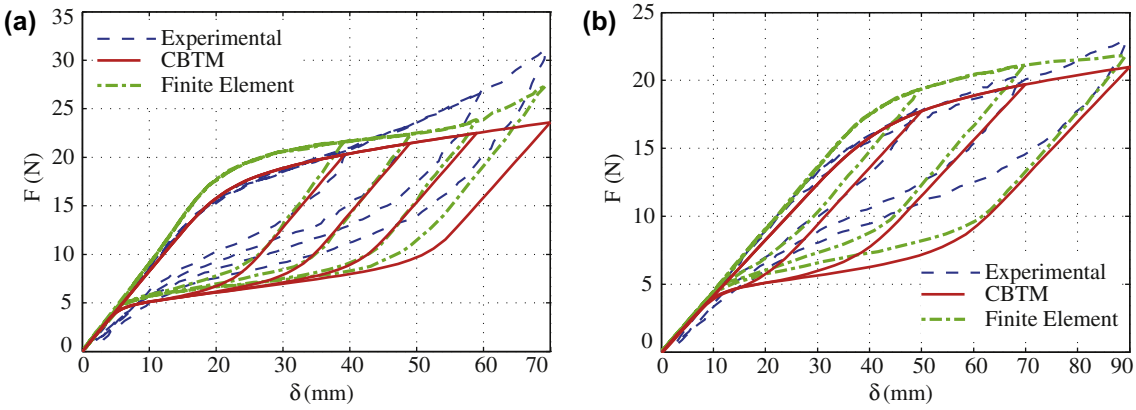

Fig. 13. Axial force versus axial displacement.

materials. The properties given in Table 1 for Material II are calibrated by comparing the results of analytical and numerical analyses with the experimental results done on the present SMA helical spring. However, in order to take the uncertainty of the material properties into consideration, we present a discussion on the effect of changing material properties on the spring response in this section. The numerical results presented in this section can also be used in designing SMA helical springs for various applications. All the numerical results in this section are presented based on CBTM and the spring is considered to be at $T = 27\ ^{\circ}C$.

Two of the material properties that have a significant influence on the SMA helical spring response in loading–unloading are the austenite and martensite elastic moduli. In practice, the elastic modulus of different SMAs covers a wide range (see Toi et al. (2004) for an SMA with $E_A = 34$ GPA, $E_M = 28.5$ GPA and Jacobus et al. (1996) for an SMA with $E_A = 72$ GPA, $E_M = 30$ GPA). The effect of a decrease and increase in the elastic moduli of a material with properties given in Table 1 is shown in Fig. 14. As it is shown in this figure, increasing E_A and E_M causes a remarkable increase in the hysteresis area that is strongly preferred for springs as energy absorbing devices. Note that this area is proportional to the amount of absorbed energy in a loading–unloading cycle.

The effects of an increase or decrease in the parameter $d\sigma/dT$ by the amounts of 15% and 30% are shown in Fig. 15. The parameter $d\sigma/dT$ is the transformation curve slope in stress–temperature space and as expressed in (13), it is related to the specific entropy difference $\rho\Delta s_0$ (see Qidwai and Lagoudas, 2000a, for more details on the physics of the material properties and for a detailed experimental technique for measuring these properties). As it is shown in Fig. 15, an increase in the parameter $d\sigma/dT$ decreases the hysteresis area but remarkably increases the spring stiffness. This figure leads to an important conclusion for designing SMA helical springs

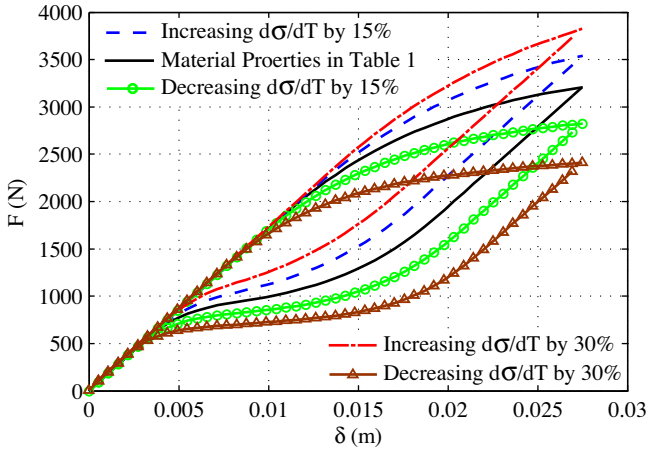

Fig. 15. The effect of change of the parameter $d\sigma/dT$ on the loading–unloading response of a shape memory alloy helical spring.

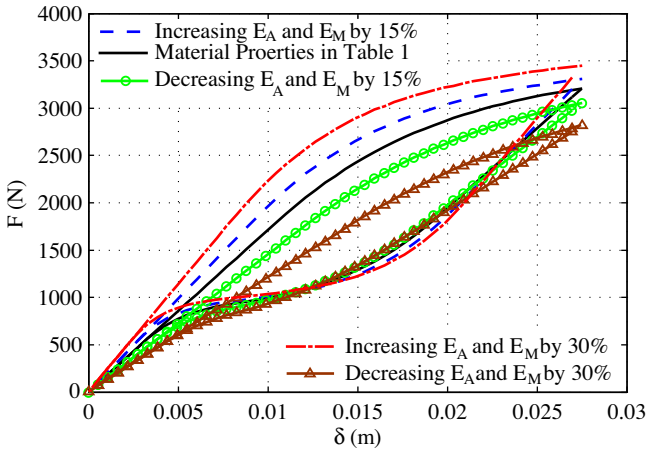

Fig. 14. The effect of change of austenite and martensite elastic moduli on the loading–unloading response of a shape memory alloy helical spring.

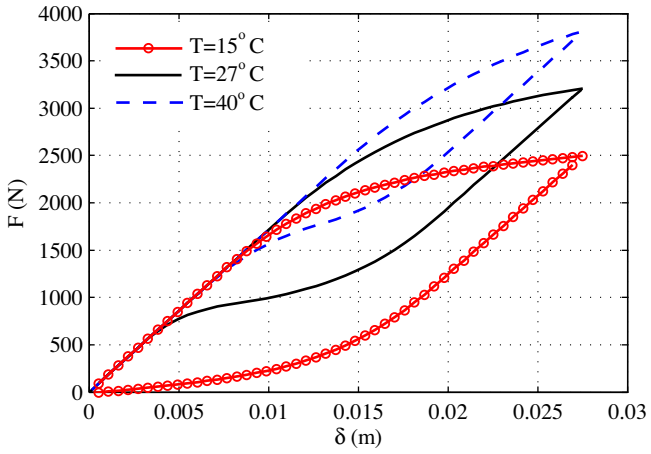

Fig. 16. The effect of temperature change on the loading–unloading response of shape memory alloy helical spring.

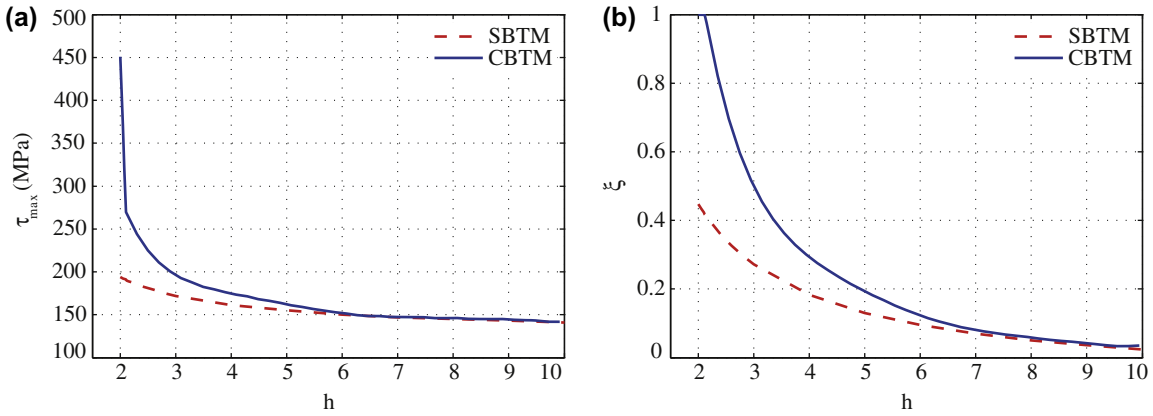

Fig. 17. Comparison between the STBM and CBTM results for (a) the maximum shear stress, and (b) the maximum volume fraction in the cross section for helical springs with various helix indices.

as energy absorbing devices. It shows that in the cases that a stiffer spring is needed, SMA materials with larger $d\sigma/dT$ are preferred while the springs made of SMA materials with lower $d\sigma/dT$ have lower stiffness and larger hysteresis area.

6.5. The effect of ambient temperature on the SMA spring response

As mentioned in Section 4, a slow loading rate is considered in the experimental and analytical analyses of the SMA helical spring in this paper. In slow loadings, the isothermal assumption is valid and the spring can be considered to be in the same temperature with the ambient environment during loading and unloading. Since one of the applications of SMA helical springs is seismic retrofit of buildings (Speicher et al., 2009), the spring may be used in various areas or at different times of a year. Therefore, it is important to study the effect of ambient temperature on the spring response. Three common temperatures are considered in Fig. 16 and the spring loading–unloading response in these temperatures is calculated (the results are obtained using CBTM). As it is shown in this figure, the ambient temperature has a considerable effect on the SMA helical spring response and at higher temperatures the hysteresis area decreases remarkably while the stiffness is increased. The spring loading–unloading cycle has a larger hysteresis area at lower temperatures but the stiffness is lower compared to higher temperatures.

6.6. CBTM and STBM for analyzing different spring geometries

As mentioned in the previous sections, introducing the curvature effect in the solution based on the torsion of straight bars for analyzing helical SMA springs (SBTM), a more accurate method (CBTM) is obtained for SMA springs with smaller indices. Because the CBTM needs an iterative procedure for finding the location of torsion centroid, it is more time consuming compared to the STBM. From a design point of view it would be interesting to find the range of spring indices for which the STBM gives acceptable accuracy and a criterion for the necessity of using CBTM. In this section an SMA helical spring with properties given in Table 1 as Material II is considered. The mean coil radius is $R_m = 2$ cm and the total length of the spring is 11 cm. The spring has five turns and it is subjected to tension causing a maximum elongation of 6 cm. The cross section radius is considered variable for obtaining different helix indices. Temperature is assumed to be $T = 300$ K. Fig. 17(a) shows the maximum shear stress in the cross section and Fig. 17(b) shows the maximum volume fraction in the cross section for different helix indices obtained by SBTM and SBTN. As it is shown in these figures decreasing the spring index, the difference between CBTM and SBTM increases. The results calculated by SBTM for both the maximum shear stress and the martensitic volume fraction deviate more than 5% from the CBTM results for the helix indices smaller than 5. This difference increases considerably for the calculated maximum shear stress for spring indices smaller than 2.12 for which CBTM predicts completion of phase transformation and a sharp increase in the shear maximum stress in the cross section.

The analysis of maximum shear stress as a function of geometric properties, e.g. the spring index for different spring geometries can also be used in a design procedure for calculating the critical geometries for which the maximum shear stress reaches a critical value. This critical value can be considered as the stress corresponding to the end of reversible stress–strain response for the SMA material. As an example, if the maximum stress in the pseudoelastic stress–strain response is $\tau_{max} = 300$ MPa, for spring indices smaller than 2.11, the maximum shear stress is more than the critical value and elongating the spring more than the considered value (6 cm) will cause a nonrecoverable overstretching (see Fig. 17(a)). Similar design graphs can be obtained by the present formulation for different geometric properties, material properties, and loading conditions.

7. Conclusions

In this paper two new strategies for analysis of SMA helical springs subjected to an axial load are presented. One is based on an exact solution for the pure torsion of a straight SMA bar and the other considers a curvature correction and uses the torsion of a curved SMA bar. In addition to the global force–displacement response, using the proposed analytical method precise stress and martensitic volume fraction distributions in the spring cross section are calculated. SMA helical springs are also analyzed using a three-dimensional finite element method. An experimental test is done on a Nitinol spring and the analytical, numerical, and experimental results are compared. It is shown that the analysis based on the curved SMA bar torsion theory can predict the stress and martensitic volume fraction in the cross section accurately. Using the proposed analytic solution, the SMA helical springs can be analyzed remarkably faster compared to finite element simulations. Having this solution, the effect of any geometrical or material property on the spring response can be studied without time limitations even in an optimization process in which a large number of simulations is required for finding an optimum. The effect of a change in material properties and the ambient temperature on the load–displacement response of the SMA helical spring is stud-

ied and practical recommendations are given for improving these springs when used as energy absorbing and damping devices. It is shown that SMA springs made of materials with larger austenite and martensite elastic moduli and lower specific entropy difference, are more efficient in dissipating energy. Also it is shown that for having stiffer springs, SMA materials with larger austenite and martensite elastic moduli and specific entropy difference should be used. Because one of the applications of SMA helical springs is energy absorption in seismic events, it is necessary to study the response of these springs to external loads applied with different rates. For studying the response of SMA helical springs in high loading rates, the latent heat effect should be considered and a coupled thermomechanical problem has to be solved.

A comprehensive study of the response of shape memory alloys by considering the effects of phase transformation induced latent heat is an important extension of the present work. To analyze the rate-dependent response of SMAs, in addition to the ambient condition, one needs to consider the latent heat generation effects. This will be the subject of a future communication.

Appendix A. Analytical expressions for shear stress in loading and unloading

In this appendix, an explicit expression for the shear stress is given. The coefficients in (19) are

$$
\begin{aligned}
F_1 &= -\frac{\sqrt{3}H}{\Delta S_{44}},\\
F_2 &= \frac{1}{4}\frac{3\Delta E H^2 + 4\Delta E \Delta S_{44} f^{\pm}(T) + 2\rho b^{\pm} E_A \Delta S_{44}}{\Delta E \Delta S_{44}^2},\\
F_3 &= \frac{\sqrt{3}}{12}\frac{6\Delta E H^2 f^{\pm}(T) + 3\rho b^{\pm} E_A H^2 + 2(1+\nu)(\rho b^{\pm})^2}{H\Delta E \Delta S_{44}^2},\\
F_4 &= \frac{1}{4}\frac{f^{\pm}(T)(\Delta E f^{\pm}(T) + \rho b^{\pm} E_A)}{\Delta E \Delta S_{44}^2},\\
F_2^* &= -\frac{1}{6}\frac{\rho b^{\pm}\sqrt{3}}{\Delta S_{44} H},\\
F_3^* &= -\frac{1}{4}\frac{\rho b^{\pm}}{\Delta S_{44}^2},\\
F_4^* &= -\frac{\sqrt{3}}{12}\frac{\rho b^{\pm}\left(\Delta E f^{\pm}(T) + \rho b^{\pm} E_A\right)}{H\Delta E \Delta S_{44}^2}
\end{aligned}
\tag{A.1}
$$

in which $\Delta E = (E_M - E_A)$. Using these constants, the following parameters are introduced:

$$
\begin{aligned}
&G_1 = -\frac{3}{8}(F_1)^2 + F_2, \quad G_1^* = F_2^*, \quad G_2 = \frac{1}{8}(F_1)^3 - \frac{1}{2}F_1F_2 + F_3,\\
&G_2^* = -\frac{1}{2}F_1F_2^* + F_3^*,\\
&G_3 = -\frac{3}{256}(F_1)^4 + \frac{1}{16}(F_1)^2F_2 - \frac{1}{4}F_1F_3 + F_4,\\
&G_3^1 = \frac{1}{16}(F_1)^2F_2^* - \frac{1}{4}F_1F_3^* + F_4^*,\\
&K_1 = -\frac{1}{12}(G_1)^2 - G_3, \quad K_1^* = -\frac{1}{6}G_1G_1^* - G_3^1, \quad K_1^{\diamondsuit} = -\frac{1}{12}(G_1^*)^2,\\
&K_2 = -\frac{1}{108}(G_1)^3 + \frac{1}{3}G_1G_3 - \frac{1}{8}(G_2)^2,\\
&K_2^* = -\frac{1}{36}(G_1)^2G_1^* + \frac{1}{3}G_1G_3^* + \frac{1}{3}G_3G_1^* - \frac{1}{4}G_2G_2^*,\\
&K_2^{\diamondsuit} = -\frac{1}{36}G_1G_1^* + \frac{1}{3}G_1^*G_3^* - \frac{1}{8}(G_2^*)^2, \quad K_2^{\circ} = -\frac{1}{108}(G_1^*)^3
\end{aligned}
\tag{A.2}
$$

and

$$
\begin{aligned}
\mathcal{R} = &-\frac{1}{2}K_2 - \frac{1}{2}K_2^* r\theta - \frac{1}{2}K_2^{\diamondsuit} r^2\theta^2 - \frac{1}{2}K_2^{\circ} r^3\theta^3\\
&+\left[\frac{1}{4}(K_2)^2 + \frac{1}{2}K_2K_2^* r\theta + \frac{1}{2}K_2K_2^{\diamondsuit} r^2\theta^2 + \frac{1}{2}K_2K_2^{\circ} r^3\theta^3\right.\\
&+\frac{1}{4}(K_2^*)^2 r^2\theta^2 + \frac{1}{2}K_2^* r^3\theta^3 K_2^{\diamondsuit} + \frac{1}{2}K_2^* K_2^{\circ} r^4\theta^4 + \frac{1}{4}\left(K_2^{\diamondsuit}\right)^2 r^4\theta^4\\
&+\frac{1}{2}K_2^{\diamondsuit}K_2^{\circ} r^5\theta^5 + \frac{1}{4}(K_2^{\circ})^2 r^6\theta^6 + \frac{1}{27}(K_1)^3 + \frac{1}{9}(K_1)^2K_1^* r\theta\\
&+\frac{1}{9}(K_1)^2K_1^{\diamondsuit} r^2\theta^2 + \frac{1}{9}K_1(K_1^*)^2 r^2\theta^2 + \frac{2}{9}K_1K_1^*K_1^{\diamondsuit} r^3\theta^3\\
&+\frac{1}{9}K_1\left(K_1^{\diamondsuit}\right)^2 r^4\theta^4 + \frac{1}{27}(K_1^*)^3 r^3\theta^3 + \frac{1}{9}(K_1^*)^2K_1^{\diamondsuit} r^4\theta^4\\
&\left.+\frac{1}{9}K_1^*\left(K_1^{\diamondsuit}\right)^2 r^5\theta^5 + \frac{1}{27}\left(K_1^{\diamondsuit}\right)^3 r^6\theta^6\right]^{\frac{1}{2}},
\end{aligned}
$$

$$
\begin{aligned}
&\mathcal{U} = (\mathcal{R})^{\frac{1}{3}}, \quad \mathcal{Q} = K_2 + K_2^* r\theta + K_2^{\diamondsuit} r^2\theta^2 + K_2^{\circ} r^3\theta^3,\\
&\alpha = G_1 + G_1^* r\theta, \quad \beta = G_2 + G_2^* r\theta,\\
&\mathcal{P} = K_1 + K_1^* r\theta + K_1^{\diamondsuit} r^2\theta^2, \quad \mathcal{Y} = -\frac{5}{6}\alpha + \mathcal{U} - \frac{1}{3}\frac{\mathcal{P}}{\mathcal{U}},\\
&\mathcal{W} = \sqrt{\alpha + 2\mathcal{Y}}.
\end{aligned}
\tag{A.3}
$$

The quartic Eq. (19) has four roots. Among these, only one satisfies the continuity condition for the shear stress distribution in the cross section. This admissible solution is expressed as:

$$
\tau_{\theta z} = \wp^{\pm}(r,\theta) = -\frac{1}{4}F_1 + \frac{1}{2}\mathcal{W} - \frac{1}{2}\sqrt{-3\alpha - 2\mathcal{Y} - 2\frac{\beta}{\mathcal{W}}},
\tag{A.4}
$$

where $\wp^+$ and $\wp^-$ are solutions for loading and unloading, respectively. In loading, $\wp^+(r,\theta)$ is calculated by considering the parameters with (+) sign in (A.1) and in unloading $\wp^-(r,\theta)$ is calculated by considering the parameters with (−) sign in (A.1).

References

Ancker, C.J., Goodier, J.N., 1958a. Pitch and curvature corrections for helical springs. Transactions of the ASME-Journal of Applied Mechanics 25, 466–470.

Ancker, C.J., Goodier, J.N., 1958b. Theory of pitch and curvature corrections for the helical springs-I (tension). Transactions of the ASME-Journal of Applied Mechanics 25, 471–483.

Ancker, C.J., Goodier, J.N., 1958c. Theory of pitch and curvature corrections for the helical springs-II (torsion). Transactions of the ASME-Journal of Applied Mechanics 25, 484–495.

Andrawes, B., DesRoches, R., 2007. Effect of hysteretic properties of superelastic shape memory alloys on the seismic performance of structures. Structural Control and Health Monitoring 14, 301–320.

Andrawes, B., DesRoches, R., 2008. Sensitivity of seismic applications to different shape memory alloy models. ASCE Journal of Engineering Mechanics 134 (2), 173–183.

Arghavani, J., Auricchio, F., Naghdabadi, R., Reali, R., Sohrabpour, S., 2010. A 3-D phenomenological constitutive model for shape memory alloys under multiaxial loadings. International Journal of Plasticity 26 (7), 976–991.

Auricchio, F., Fugazza, D., DesRoches, R., 2006. Numerical and experimental evaluation of the damping properties of shape-memory alloys. Journal of Engineering Materials and Technology-Transactions of the ASME 128 (3), 312–319.

Bo, Z., Lagoudas, D.C., 1999. Thermomechanical modeling of polycrystalline SMAs under cyclic loading, Part I: Analytical derivations. International Journal of Engineering Science 37, 1089–1140.

Boyd, J.G., Lagoudas, D.C., 1996. A thermodynamic constitutive model for the shape memory alloy materials. Part I. The monolithic shape memory alloy. International Journal of Plasticity 12, 805–842.

Brinson, L.C., 1993. One-dimensional constitutive behavior of shape memory alloy: thermomechanical derivation with non-constant material functions and redefined martensite internal variable. Journal of Intelligent Material Systems and Structures 4, 229–242.

Brook, G.B., 1983. Applications of titanium–nickel shape memory alloys. Materials and Design 4 (4), 835–840.

Cardano, G., Witmer, T.R., Ore, O., 2007. The Rules of Algebra: (ars Magna). Dover Publications.

Chang, L.C., Read, T.A., 1951a. Plastic deformation and diffusionless phase changes in metals – the gold-cadmium beta-phase. Transactions of the American Institute of Mining and Metallurgical Engineering 191 (1), 47–52.

Chang, L.C., Read, T.A., 1951b. Experimental evidence of relaxation diffusionless phase changes of single crystal beta-AU-CD alloys containing 47.5 atomic percent CD. Physical Review 82 (5), 770.
Chen, T., 2004. A homogeneous elliptical shaft may not warp under torsion. Acta Mechanica 169, 221–224.
DesRoches, R., Delemont, M., 2002. Seismic retrofit of simply supported bridges using shape memory alloys. Engineering Structures 24, 325–332.
DesRoches, R., Smith, B., 2004. Shape memory alloys in seismic resistant design and retrofit: a critical review of their potential and limitations. Journal of Earthquake Engineering 8, 415–429.
Dong, Y., Boming, Z., Jun, L., 2008. A changeable aerofoil actuated by shape memory alloy springs. Materials Science and Engineering A 485, 243–250.
Goldberg, D.E., 1989. Genetic Algorithms in Search, Optimization, and Machine Learning. Addison-Wesley, London.
Hartl, D.J., Lagoudas, D.C., 2007. Aerospace applications of shape memory alloys. Proceedings of the IMechE Part G: Journal of Aerospace Engineering 221, 535–552.
Higgins, T.J., 1942. A comprehensive review of Saint-Venant's torsion problem. American Journal of Physics 10 (5), 248–259.
Jacobus, K., Sehitoglu, H., Balzer, M., 1996. Effect of stress state on the stress-induced martensitic transformation in polycrystalline NiTi alloy. Metallurgical and Materials Transactions A 27, 3066?73.
Jee, K.K., Hana, J.H., Jang, W.Y., 2006. A method of pipe joining using shape memory alloys. Materials Science and Engineering A 438–440, 1110–1112.
Kastner, O., 2003. Molecular-dynamics of a 2D model of the shape memory effect-Part I: Model and simulations. Continuum Mechanics and Thermodynamics 15, 487–502.
Kastner, O., 2006. Molecular-dynamics of a 2D model of the shape memory effect-Part II: Thermodynamics of a small system. Continuum Mechanics and Thermodynamics 18, 63–81.
Lagoudas, D.C. (Ed.), 2008. Shape Memory Alloys: Modeling and Engineering Applications. Springer, New York.
Lee, C.Y., Zhuo, H.C., Hsu, C.W., 2009. Lateral vibration of a composite stepped beam consisted of SMA helical spring based on equivalent Euler–Bernoulli beam theory. Journal of Sound and Vibration 324, 179–193.
Liang, C., Rogers, C.A., 1992. The multi-dimensional constitutive relations of shape memory alloys. Journal of Engineering Mathematics 26, 429–443.
Liang, C., Rogers, C.A., 1997. Design of shape memory alloy springs with applications in vibration control. Journal of Intelligent Material Systems and Structures 8 (4), 314–322.
McCormick, J., DesRoches, R. 2006. The Effect of training, pre-straining, and loading history on the properties of NiTi shape memory alloys for protective systems in civil engineering. In: Proceedings of the ASCE Structures Congress, St. Louis, MO., April, 2006.
McCormick, J., DesRoches, R., Fugazza, D., Auricchio, F., 2006. Seismic vibration control using superelastic shape memory alloys. Journal of Engineering Materials and Technology-Transactions of the ASME 128 (3), 294–301.
Mirzaeifar, R., Shakeri, M., Sadighi, M., 2009. Nonlinear finite element formulation for analyzing shape memory alloy cylindrical panels. Smart Materials and Structures 18 (3), 035002.
Mirzaeifar, R., DesRoches, R., Yavari, A., 2010. Exact solutions for pure torsion of shape memory alloy circular bars. Mechanics of Materials 42 (8), 797–806.
Mirzaeifar, R., Shakeri, M., DesRoches, R., Yavari, A., in press. A semi-analytic analysis of shape memory alloy thick-walled cylinders under internal pressure. Archive of Applied Mechanics. doi:10.1007/s00419-010-0468-x.
Müller, I., Seelecke, S., 2001. Thermodynamic aspects of shape memory alloys. Mathematical and Computer Modelling 34 (12–13), 1307–1355.
Müller, I., Xu, H., 1991. On the pseudo-elastic hysteresis. Acta Metallurgica Matereralia 39 (3), 263–271.
Papadimitriou, C.H., Steiglitz, K., 1982. Combinatorial Optimization: Algorithms and Complexity. Prentice-Hall, Englewood Cliffs, NJ.
Petrini, L., Migliavacca, F., Massarotti, P., Schievano, S., Dubini, G., Auricchio, F., 2005. Computational studies of shape memory alloy behavior in biomedical applications. Journal of Biomechanical Engineering 127, 716–725.
Popov, P., Lagoudas, D.C., 2007. A 3-D constitutive model for shape memory alloys incorporating pseudoelasticity and detwinning of self-accommodated martensite. International Journal of Plasticity 23, 1679–1720.
Qidwai, M.A., Lagoudas, D.C., 2000a. On thermomechanics and transformation surfaces of polycrystalline NiTi shape memory alloy material. International Journal of Plasticity 16, 1309–1343.
Qidwai, M.A., Lagoudas, D.C., 2000b. Numerical implementation of a shape memory alloy thermomechanical constitutive model using return mapping algorithms. International Journal for Numerical Methods in Engineering 47, 1123–1168.
Sokolnikoff, I.S., 1956. Mathematical Theory of Elasticity. McGraw-Hill, New York.
Speicher, M., Hodgson, D.E., DesRoches, R., Leon, R.T., 2009. Shape memory alloy tension/compression device for seismic retrofit of buildings. Journal of Materials Engineering and Performance 18, 746–753.
Tanaka, K., 1986. A thermomechanical sketch of shape memory effect: one-dimensional tensile behavior. Res Mechanica 18 (3), 251–263.
Tanaka, K., Nishimura, F., Hayashi, T., Tobushi, H., Lexcellent, C., 1995. Phenomenological analysis on subloops and cyclic behavior in shape memory alloys under mechanical and/or thermal loads. Mechanics of Materials 19, 281–292.
Tanaka, Y., Himuro, Y., Kainuma, R., Sutou, Y., Omori, T., Ishida, K., 2010. Ferrous polycrystalline shape-memory alloy showing huge superelasticity. Science 327, 1488–1490.
Tobushi, H., Tanaka, K., 1991. Deformation of a shape memory alloy helical spring: analysis based on stress–strain–temperature relation. JSME International Journal, Series I 34, 83–89.
Toi, Y., Lee, J.B., Taya, M., 2004. Finite element analysis of superelastic, large deformation behavior of shape memory alloy helical springs. Computers and Structures 82, 1685–1693.
Voit, W., Ware, T., Dasari, R.R., Smith, P., Danz, L., Simon, D., Barlow, S., Marder, S.R., Gall, K., 2010. High-strain shape-memory polymers. Advanced Functional Materials 20, 162–171.
Wahl, A.M., 1944. Mechanical Springs. Penton Publishing Company, Clevland, Ohio.
Xua, M.B., Song, G., 2004. Adaptive control of vibration wave propagation in cylindrical shells using SMA wall joint. Journal of Sound and Vibration 278, 307–326.